RSC Advances

PAPER

View Article Online
View Journal | View Issue

Cite this: *RSC Adv.*, 2023, **13**, 34497

Advancing nitrate reduction to ammonia: insights into mechanism, activity control, and catalyst design over Pt nanoparticle-based ZrO_2†

Ayyaz Mahmood,[abcd] Fouzia Perveen,[e] Tehmina Akram,[f] Shenggui Chen,*[bcd] Ahmad Irfan[g] and Huafu Chen*[a]

The reduction of nitrogen oxides (NO_x) to NH_3, or N_2 represents a crucial step in mitigating atmospheric NO_3 and NO_2 emissions, a significant contributor to air pollution. Among these reduction products, ammonia (NH_3) holds particular significance due to its utility in nitrogen-based fertilizers and its versatile applications in various industrial processes. Platinum-based catalysts have exhibited promise in enhancing the rate and selectivity of these reduction reactions. In this study, we employ density functional theory (DFT) calculations to explore the catalytic potential of Pt nanoparticle (PtNP)-supported ZrO_2 for the conversion of NO_3 to NH_3. The most favorable pathway for the NO_3 reduction to NH_3 follows a sequence, that is, $NO_3 \rightarrow NO_2 \rightarrow NO \rightarrow ONH \rightarrow ONH_2/HNOH \rightarrow NH_2/NH \rightarrow NH_2 \rightarrow NH_3$, culminating in the production of valuable ammonia. The introduction of low-state Fe and Co dopants into the ZrO_2 support reduces energy barriers for the most challenging rate-determining hydrogenation step in NO_x reduction to NH_3, demonstrating significant improvements in catalytic activity. The incorporation of dopants into the ZrO_2 support results in a depletion of electron density within the Pt cocatalyst resulting in enhanced hydrogen transfer efficiency during the hydrogenation process. This study aims to provide insights into the catalytic activity of platinum-based ZrO_2 catalysts and will help design new high-performance catalysts for the reduction of atmospheric pollutants and for energy applications.

Received 22nd September 2023
Accepted 10th November 2023

DOI: 10.1039/d3ra06449b

rsc.li/rsc-advances

1. Introduction

Nitrogen oxides (NO_x) are significant pollutants in the atmosphere, primarily originating from the combustion of fossil fuels, including coal.[1] As a major consumer of coal, China faces the challenge of substantial NO_x emissions during combustion, leading to their release into the atmosphere. These emissions, combined with particulate matter, contribute to the occurrence of severe smog in northern regions of China, posing a serious threat to public health.[2,3] Among the NO_x gases, nitrogen dioxide (NO_2) is an inorganic air pollutant that poses significant harm to human health, animals, and the environment.[1,4,5] While natural events such as volcanic eruptions, lightning strikes, and forest fires also contribute to NO_x emissions, the most substantial sources are human activities, including combustion processes, transportation, and industrial operations.[1] When NO_2 is exposed to sunlight, it undergoes photolysis, breaking down into nitrogen monoxide (NO) and atomic oxygen, $O(^3P)$. The atomic oxygen then combines with molecular oxygen to form tropospheric ozone.[6] This process plays a crucial role in the formation of photochemical smog, which consists of a harmful mixture of toxic chemicals resulting from the interaction between NO_x and volatile organic compounds (VOCs). Exposure to photochemical smog, including elevated levels of tropospheric ozone, can have detrimental effects on the respiratory system and overall lung health.[5,7]

On the other hand, over the past century, the widespread use of artificial nitrogen fertilizers has significantly increased food

[a]*School of Life Science and Technology, University of Electronic Science and Technology, Chengdu 610054, China. E-mail: chenhf@uestc.edu.cn*
[b]*School of Mechanical Engineering, Dongguan University of Technology, Dongguan 523808, China. E-mail: dgutchensg@163.com*
[c]*School of Art and Design, Guangzhou Panyu Polytechnic, Guangzhou 511483, China*
[d]*Dongguan Institute of Science and Technology Innovation, Dongguan University of Technology, Dongguan 523808, China*
[e]*School of Interdisciplinary Engineering & Sciences (SINES), National University of Sciences and Technology (NUST), Sector H-12, Islamabad, 44000, Pakistan*
[f]*CAS Key Laboratory of Soft Matter Chemistry, Hefei National Laboratory for Physical Sciences at Microscale, Collaborative Innovation Center of Chemistry for Energy Materials (iChEM), Department of Chemistry, University of Science and Technology of China, Hefei 230026, China*
[g]*Department of Chemistry, College of Science, King Khalid University, P.O. Box 9004, Abha 61413, Saudi Arabia*

† Electronic supplementary information (ESI) available: Figures of optimized geometries of various intermediates and transition states involved in reactions on Pt_{11}/ZrO_2 catalyst, AIMD trajectory and Tables for energy barrier with coverage effect and Bader charge analyses. The supplementary material is available free of charge on the journal website as pdf file. See DOI: https://doi.org/10.1039/d3ra06449b

production, but it has also led to environmental challenges on a global scale. Eutrophication and acidification of water resources are among the issues caused by the excessive presence of high-valence-state nitrate, which is highly toxic to both humans and the environment.[8,9] To mitigate these problems, the World Health Organization (WHO) has set strict guidelines recommending a maximum nitrate concentration of 50 mg dm^{-3} in drinking water.[10] Unfortunately, the contamination of underground water sources due to the excessive emission of nitrate ions has become a widespread issue caused by factors such as fertilizer runoff, stock farming, and industrial wastewater.[11,12] To combat this problem, there is a growing need to develop efficient methods for converting toxic nitrate into valuable ammonia. Ammonia, with its low-valence-state, is not only an essential component for nitrogen-based fertilizers but also serves as a key chemical in the production of artificial fibers.[13–15] Currently, the synthesis of ammonia involves the energy-intensive Haber–Bosch process, which requires high pressures and temperatures.[16] In contrast, the conversion of toxic nitrate into ammonia in a catalytic reduction process holds significant scientific and practical importance. By developing a catalytic system for the reduction of nitrate, it becomes possible to convert harmful nitrate compounds into valuable ammonia. This process offers several benefits, including its potential contribution to the ecosystem, improvement of human health, and facilitation of sustainable social development.

Photocatalysis offers a promising and sustainable approach to facilitate the process.[17,18] Various photocatalysts, including TiO_2, $SrTiO_3$, and BiOCl, have been investigated for their ability to catalyze the reduction of NO_3^- into NH_3.[19–21] Furthermore, the deposition of metal particles, such as Cu, Au, Ag, Pt, and Pd, has been extensively employed to enhance both the catalytic performance and visible light absorption characteristics of Catalysts/TiO_2.[22–25] This strategy effectively suppresses electron–hole recombination and promotes photocatalytic activity. For example, Yamauchi *et al.* successfully achieved high NH_3 selectivity of approximately 78% in the photocatalytic reduction of NO_3^- by depositing alloyed CuPd nanoparticles on TiO_2.[25] However, the electron-rich nature of TiO_2 tends to promote the undesired oxidation of NO_2 to NO_3^- species rather than the desired reduction to nitrogen-containing compounds. This is due to the ability of TiO_2 to stabilize intermediate NO_2 adsorbates and facilitate their oxidation through a bifunctional charge exchange mechanism. The stabilization of surface-NO_3^- and NO_3^- ion pair configurations on TiO_2 further supports the notion that TiO_2 may be more favorable for NO_2 oxidation reactions rather than its reduction to nitrogen-containing compounds.

Multicomponent catalyst systems, which comprise two or more interdependent components, have gained recognition as promising materials for achieving higher catalytic activities. One approach involves the utilization of oxide-supported metals, which operate through the interfacial effect at the interfaces between the oxide and metal components.[26–29] Significant efforts have been devoted to the exploration of active metals for these multicomponent catalyst systems, ranging from precious platinum-group metals to nonprecious transition metals. The objective is to identify suitable catalysts that can effectively promote the desired chemical reactions. Meanwhile, there is a wide range of oxide supports available for catalyst systems, including ZnO, Al_2O_3, ZrO_2, SiO_2, TiO_2, CeO_2, Ga_2O_3, MgO, Cr_2O_3, and Nb_2O_5. In these systems, metals are commonly recognized as the active sites. The properties of metals, such as particle size, dispersion, specific surface area, and alloy components, along with their interactions with the supports, have been extensively discussed in various reviews and perspective articles. These studies aim to establish correlations between these metal and support properties and the catalytic performance of the systems.[30–37]

Zirconium dioxide (ZrO_2) is highly valued as both a catalyst and support material for various reactions due to its exceptional thermal stability, excellent redox properties, and the presence of acid–base sites on its surface. It has been successfully utilized in reactions such as CO_2 methanation,[38,39] water–gas shift,[40,41] and NO_2 selective catalytic reduction.[42,43] Particularly noteworthy is the powerful catalytic activity exhibited by transition metal oxides dispersed on the surface of ZrO_2 in NO reduction reactions. Studies have shown that Cu/ZrO_2 catalysts demonstrate high NO conversion to N_2 at low temperatures, utilizing a nitrous oxide (N_2O) intermediate in the NO–CO reaction.[44] ZrO_2, as a support material, outperforms CeO_2 in reducing the energy barrier for NO dissociation.[45] Additionally, ZrO_2 offers ample sites for NO_x adsorption, which is beneficial for NO reduction.[46,47] Notably, a study by Koga *et al.* discovered that a c-ZrO_2 (110) ultrathin film covering a Cu surface exhibited remarkable activity in NO_x reduction.[48]

Among metal supports, Pt is widely recognized as a versatile catalyst and finds extensive use in both experimental studies and industrial applications. It serves as a cocatalyst in various photocatalytic reduction reactions, including water splitting for hydrogen production,[49–52] CO_2 reduction,[53–55] and NO_3^- reduction processes.[56–58] Additionally, Pt is extensively employed in electrocatalytic NO_3^- reduction processes aimed at producing NH_3. Previous studies by Dima and Figueiredo, as well as their colleagues, demonstrated the catalytic activity of pure Pt electrodes in the reduction of NO_3^- in acidic solutions, proposing adsorbed NO as the reactive intermediate in NH_3 formation.[57,58] Moreover, Cerron-Calle *et al.* achieved a remarkably high NH_3 selectivity of 94% by utilizing alloyed CuPt catalysts for electrocatalytic NO_3^- reduction.[56] Considering Pt's excellent ability to provide surface-active H* in photocatalysis and catalyze NO_3^- reduction in electrocatalysis, it is reasonable to speculate that Pt/ZrO_2 would serve as an excellent model system for investigating the photocatalytic reduction of NO_3^- to NH_3.

Although significant experimental progress has been made in the field of nitrate reduction to ammonia, there are still gaps in our understanding of the underlying mechanistic details, rate-determining steps, and catalyst regulation strategies. One particular area of debate revolves around the conversion of nitric oxide (NO) into ammonia (NH_3), which is considered a crucial intermediate in the process. Clayborne *et al.* proposed a pathway where NH_3 is formed through the intermediate NOH*. According to their suggested mechanism, the favorable

sequence involves the conversion of NO to NOH, followed by N, NH, NH_2, and finally NH_3.[59] In contrast, Koper *et al.* presented an alternative perspective, suggesting that ammonia is produced through the intermediates HNO* and H_2NO*. Their proposed pathway starts with the conversion of NO to HNO, then H_2NO, and finally NH_3.[60] Additionally, Cuesta *et al.* put forward the idea that the intermediate HNOH* plays a pivotal role in NO reduction, suggesting a pathway of NO to NOH (HNO), then HNOH, and ultimately NH_3.[61]

Clearly, there is ongoing debate and multiple proposed pathways for the conversion of NO to NH_3 in nitrate reduction. To improve the efficiency of this process, it is imperative to dedicate further efforts towards understanding the complete reaction mechanism, including the energetics and intermediates involved. Advancements in this area will contribute to refining the catalyst design and optimization strategies, ultimately leading to enhanced nitrate reduction efficiency and the production of valuable ammonia.

Thus, in this context, we employed density functional theory (DFT) calculations to systematically investigate the process of NO_3^- reduction to NH_3 on a Pt nanoparticle (PtNP)/ZrO_2 composite model. Our previous research (under review) involved extensive *ab initio* molecular dynamics (AIMD) simulations, which allowed us to determine the PtNP/ZrO_2(111) composite structures (Fig. S2†).[62] Based on the stability, hydrogen evolution reaction (HER) and water-splitting reaction (WSR) activities, Pt_{11}/ZrO_2 was chosen for current study. First, we examined the reaction energetics of various elementary steps within different potential pathways of NO_3^- reduction. Through this analysis, we identified the most favorable pathway and determined the rate-determining steps. Next, we explored the effect of charge density modulation on the NO_3^- reduction activity by manipulating the PtNP's charge density on the ZrO_2 support. By understanding the trend in activity variation, we proposed a strategy to enhance the catalytic performance of PtNP/ZrO_2 by doping ZrO_2 with a suitable element, such as Fe and Co. This proposed modification was supported by our calculated results, which indicated a significant reduction in reaction barriers and an increase in energy gains. Overall, our study provides valuable insights into the NO_3^- reduction mechanism on PtNP/ZrO_2 catalysts, offering a potential avenue for improving catalytic performance through targeted modifications. The findings from this study will contribute to the understanding and development of advanced catalyst materials for efficient NO_3 reduction, with potential applications in automotive emission control systems and industrial processes. Ultimately, the utilization of Pt nanoparticle-based ZrO_2 catalysts holds promise for mitigating the adverse effects of NO_3/NO_2 pollution and promoting cleaner and healthier environments.

2. Methods

In this study, computational simulations were performed using the BAND module of the Amsterdam Modeling Suite (AMS) developed by Software for Chemistry & Materials BV (SCM).[63,64] The simulations employed the linear combination of atomic orbitals (LCAO) approach[65] and the generalized gradient approximation (GGA) with the Perdew–Burke–Ernzerhof (PBE) functional within the framework of density functional theory (DFT).[66,67] To describe the atomic structures, a combination of valence triple-zeta polarized (TZP) Slater-type orbitals and Herman–Skillman numerical atomic orbitals (NAOs) with a small frozen core was utilized. The van der Waals (vdW) interactions were accounted by using Grimme's third-generation dispersion correction together with Becke–Johnson damping function (D3-BJ).[68] The Pt_{11}/ZrO_2 structure was chosen for this investigation based on the results presented in our previous study which explored the effect of size of nanoparticle size on the catalytic activity determining Pt_{11} to be the optimal nanoparticle size.[62] The size of nanoparticles can significantly influence catalyst activity. Smaller nanoparticles may have fewer active sites, potentially limiting their catalytic efficiency, while larger nanoparticles might suffer from decreased charge transfer efficiency, potentially hindering their performance due to increased surface recombination. Our findings suggest that Pt_{11}/ZrO_2 strikes a balance between these factors. It provides an adequate surface area with numerous active sites, facilitates efficient charge transfer, and minimizes surface recombination, yielding the best catalyst activity.

For geometry optimizations, a maximum gradient threshold of 0.03 eV $Å^{-1}$ was employed. The convergence criteria for the electronic self-consistent loop were 10^{-6} eV which is benchmark in many studies. Relativistic effects, including spin–orbit coupling, were considered using the zero-order regular approximation (ZORA) method. Periodic boundary conditions were applied to represent the repeating unit cell structure, with a (111) surface model constructed using a 3×3 supercell containing two ZrO_2 trilayers (O–Zr–O layer). A vacuum spacing of 15 Å was set between the slabs, and a Monkhorst–Pack scheme with a $6 \times 6 \times 1$ *k*-point sampling was used to sample the Brillouin zone.[69] Dipole correction was applied in all calculations. The bottom ZrO_2 trilayer was held fixed at its bulk positions, while the top ZrO_2 trilayer and the adsorbents were allowed to fully relax to reach their equilibrium structures. To determine the stable representative configuration of Pt_{11} cluster on ZrO_2, we employed AIMD simulations. The simulations utilized Nosé–Hoover thermostats in the canonical (NVT) ensemble for over 20 ps, achieving equilibrium around 10 ps. Structural configurations were selected at 1 ps intervals from the equilibrated trajectory and fully optimized to minimize all forces. Out of 10 potential structural candidates, we determined optimal Pt_{11}/ZrO_2 structures based on their lowest energy.

Transition states associated with the water-splitting reactions were determined by systematically exploring the potential energy surface (PES) along the relevant reaction coordinates. The PES was scanned to identify the highest energy point, which was then optimized to obtain the transition state structure.[70] The forces threshold for the transition state search was set to 0.05 eV $Å^{-1}$. To validate the transition states, it was ensured that they exhibited only one imaginary frequency along the reaction coordinate.[71,72] The vibrational modes were calculated using similar methods as for optimizations. They were specifically computed for the cluster and reacting species on the cluster,

excluding the ZrO_2 substrate for computational efficiency. The finite differences method was employed to calculate the vibrational frequencies, utilizing a step length of 0.005 Å. The Gibbs free energies of reaction (ΔG_r) and Gibbs activation energy barriers ($\Delta^{\ddagger}G$) for the water-splitting reaction were calculated as the differences in free energy between the involved species, as described by eqn (1) and (2), respectively.

$$\Delta G_r = \Delta G_{Products} - \Delta G_{reactants} \quad (1)$$

$$\Delta^{\ddagger}G = \Delta G_{TS} - \Delta G_{reactants} \quad (2)$$

3. Results and discussion

We chose Pt_{11}/ZrO_2 composite as the substrate to represent the Pt nanoparticle-based ZrO_2 catalyst which was obtained from *ab initio* molecular dynamics (AIMD) simulations (Fig. S2†) presented in our previous study which investigates the size effect of Pt nanoparticles on the catalytic activity.[62] To maintain a neutral charge in our simulation, we introduced a $NaNO_3$ molecule into the system to represent the NO_3^- ion. We positioned the Na^+ cation of the $NaNO_3$ molecule uniformly on the opposite (bottom) layer of the ZrO_2 slab and allowed it to relax (Fig. 1 and S1†). Bader charge calculations (Table S1†) reveal that the Pt_{11} cluster possesses an overall positive charge of +0.72 |e|, with an average charge of +0.067 |e| on each Pt atom within the cluster. When negatively charged NO_3^- species are introduced, the total charge decreases by 0.48 |e|, leading to a net charge of −0.22 |e| on the cluster. This charge is subsequently neutralized by the presence of Na^+ ions, restoring the total charge to +0.72 |e|. In essence, the cluster's charge is initially reduced by the introduction of NO_3^-, but it returns to its original positive state due to the compensating effect of Na^+ ions. Based on the adsorption energies and stability of various adsorption configurations of NO_3^- on different adsorption sites, we identified the most stable adsorption structure for NO_3^- (E_{ads} (NO_3^-) = −1.52 eV) relative to a desorbed NO_3^- in the gas phase, with Na^+ positioned on the opposite layer which is presented in Fig. 1.

In this adsorption configuration, NO_3^- forms specific bonds with Zr atoms on the ZrO_2 surface. Two O–Pt (O^1–Pt^1 and O^2–Pt^1) bonds were formed with the same Pt atom, with bond lengths of 2.196 Å and 2.461 Å, respectively. Furthermore, considering the unique properties of the ZrO_2 surface, such as its high thermal stability and acid–base characteristics, we simulated the subsequent reduction of NO_3^- under conditions where reactive hydrogen species (H*) are adequately available on the ZrO_2 surface in the form of water molecules which release protons.

3.1. *NO_3^- reduction to *NO_2

We investigated the process of *NO_3^- reduction to *NO_2 by analyzing three possible pathways for breaking the first N–O bond in NO_3^-* (as shown in Fig. 2). The first pathway is direct NO_3^* dissociation (referred to as direct NO_3^- dis., represented by the red curve). In this pathway, *NO_3^- dissociates directly into *NO_2 and *O by overcoming an energy barrier of 0.76 eV, with a significant exothermic reaction energy of −0.67 eV. The second pathway, denoted as O_2N–OH* dissociation (HO–NO_2 dis., represented by the blue curve), involves the capture of a hydrogen specie (H*) by *NO_3 to form *O_2N–OH on the surface of the catalyst. Importantly, the first hydrogenation steps are mostly characterized by an extremely low energy requirement, rendering it spontaneous. Subsequently, the formed O_2N–OH* species dissociates into NO_2* and OH* with a barrier of 0.62 eV, accompanied by a substantial energy release of −0.94 eV.

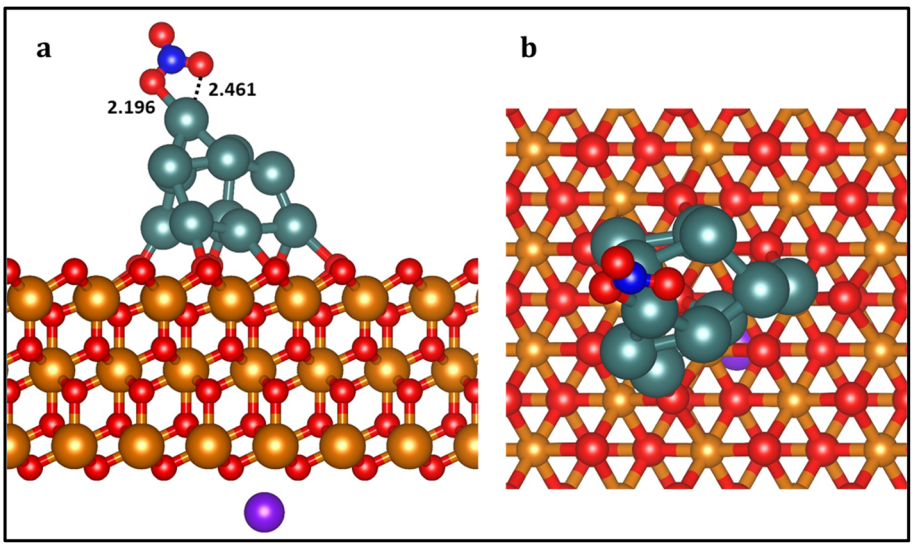

Fig. 1 Side (a) and top (b) view of the calculated most stable structure of NO_3 on Pt_{11}/ZrO_2 composite. Bond distances values in Angstrom (Å). Zr: orange; O: red; Pt: dark cyan; N: dark blue; Na^+: purple. This color scheme is used throughout the paper. The radius of Zr atoms in the top view is reduced for clarity.

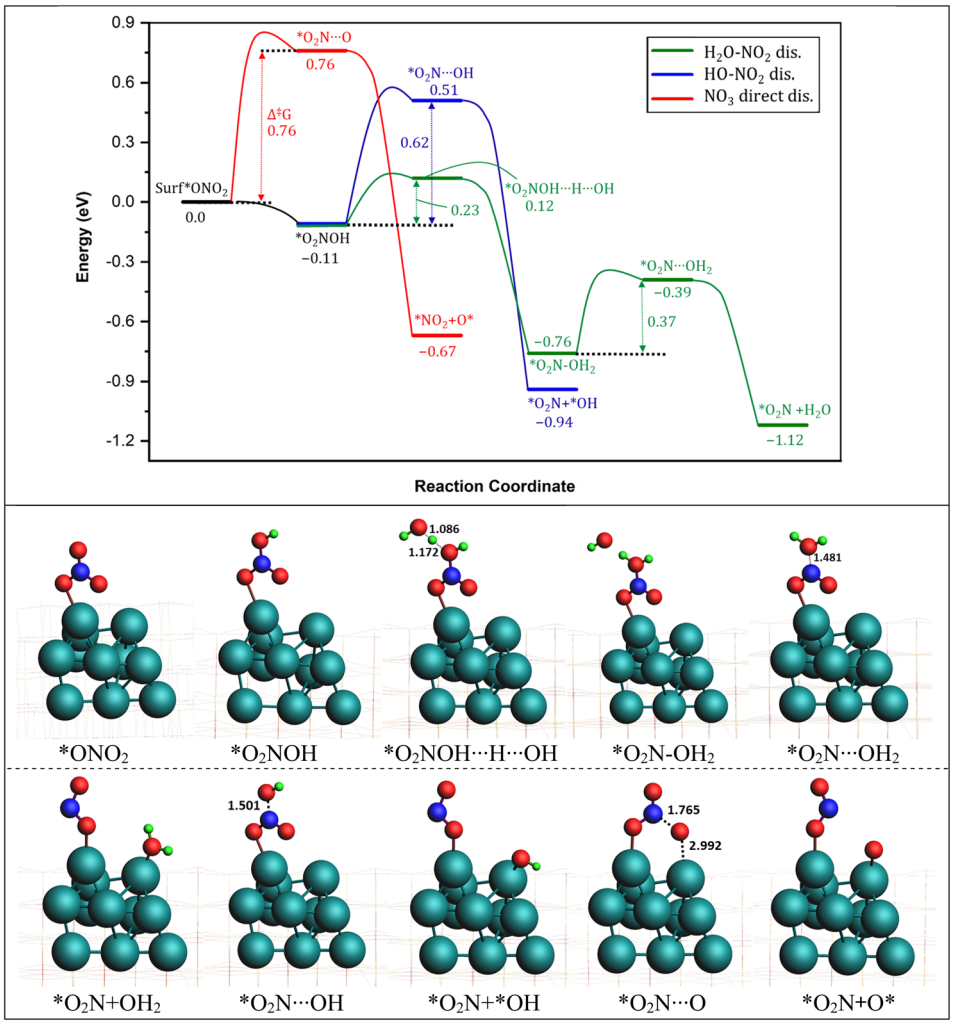

Fig. 2 (Top) reaction energy profile for the conversion pathway of NO_3^- into NO_2. Green: H_2O–NO_2 dissociation, blue: HO–NO_2 dissociation, red: NO_3^- direct dissociation. The energy of the entering or leaving species was discounted from the total energy of the system to calculate the relative energy. The energy of the H was calculated as 1/2 of the energy of H_2. (Bottom) optimized structures of various intermediates and transition states involved in the reaction pathways. ZrO_2 layers are represented by wireframes for clarity. Energy values in eV. Bond distances in Å. Similar colors were used for intermediates names.

A third pathway involves the capture of a 2nd proton by the O_2N–OH ($\Delta^{\ddagger}G$ 0.23) formed in the 2nd pathway to form the water molecule $*O_2N$–OH_2 specie (H_2O–NO_2 dis., represented by the green curve). In the next step, water molecule (H_2O) detaches with a reaction energy barrier of 0.37 eV passing through the transition state $*O_2N\cdots H_2O$. This step is calculated to be exothermic with an energy release of 0.36 eV with an overall energy release in this pathway to be −1.12 eV, indicating the most exothermic pathway for the conversion of $*NO_3$ into $*NO_2$.

These results indicate that all three pathways are feasible for the reduction of $*NO_3$ to $*NO_2$. The NO_3 direct dissociation pathway involves a higher energy barrier (0.76 eV) but offers a larger energy release upon completion. In contrast, the HO–O_2N dissociation pathway involves a lower energy barrier (0.37 eV) but a slightly smaller energy release. The bond lengths associated with the breaking N–O bond in the NO_3 direct dissociation pathway and the HO–O_2N dissociation pathway were analyzed (as shown in Fig. 1). It was observed that the distance of the breaking N–O bond in the direct NO_3 direct dissociation pathway ($*O_2N\cdots O$: 1.765 Å) is significantly longer compared to that in the HO–NO_2 dissociation pathway ($*O_2N\cdots OH_2$: 1.481 Å). Based on both the reaction energetics and the transition-state structures, it can be concluded that the H*-assisted HO–O_2N dissociation pathway is more favorable (0.37 *vs.* 0.76 eV) than the direct NO_3 dissociation pathway on the ZrO_2 surface. The calculated difference in the activation energies between both pathways is probably due to the fact that the transition states ($*O_2N\cdots OH_2$: 1.481 Å) found in O_2N–OH dissociation pathway are early transition states because they resemble more the reactants and according to the Hammond postulate the early transition states are generally characteristic of fast exothermic reactions.[73] On the other hand, the transition states ($*O_2N\cdots O$: 1.765 Å) found in the NO_3 direct dissociation

pathway are late transition states as they resemble more the products, and thus are characteristic of slow endothermic reactions. This finding is consistent with previous reports indicating the preference for the H*-assisted pathway in the reduction of $*NO_3$.[74,75]

3.2. $*NO_2$ reduction to *NO

The pathways for the dissociation of the second N–O bond in NO_2 were investigated next. Three possible routes were considered: the NO_2 direct dissociation pathway, and two H*-assisted dissociation pathways, as depicted in Fig. 3. In the NO_2 direct dissociation pathway (red curve), breaking the N–O bond requires overcoming a substantial energy barrier of 1.17 eV. Although the formation of *NO and O* releases energy (−0.28 eV), the initial bond breaking step is energetically demanding. In the *H-assisted dissociation pathways, we explored the involvement of H* in facilitating the dissociation process. It was observed that the O-end of NO_2* readily captures H* and forms *NO–OH on the Pt surface with a small energy change of 0.09 eV. Subsequently, the dissociation of *NO–OH into *NO and *OH occurs with a large barrier of 0.68 eV and a significant energy release of −0.56 eV. The overall pathway is calculated to be exothermic with a large free energy of the reaction of −0.65 eV.

A third possible pathway involves the capture of a second proton by the *NO–OH species that is formed in the second pathway, leading to the formation of a water molecule called $*NO–OH_2$. In the subsequent step, the water molecule (H_2O) undergoes detachment, with a reaction energy barrier of 0.42 eV, as it passes through the transition state $*NO\cdots H_2O$. This step is calculated to be exothermic, releasing an energy of 0.30 eV. Overall, this pathway exhibits a significant energy

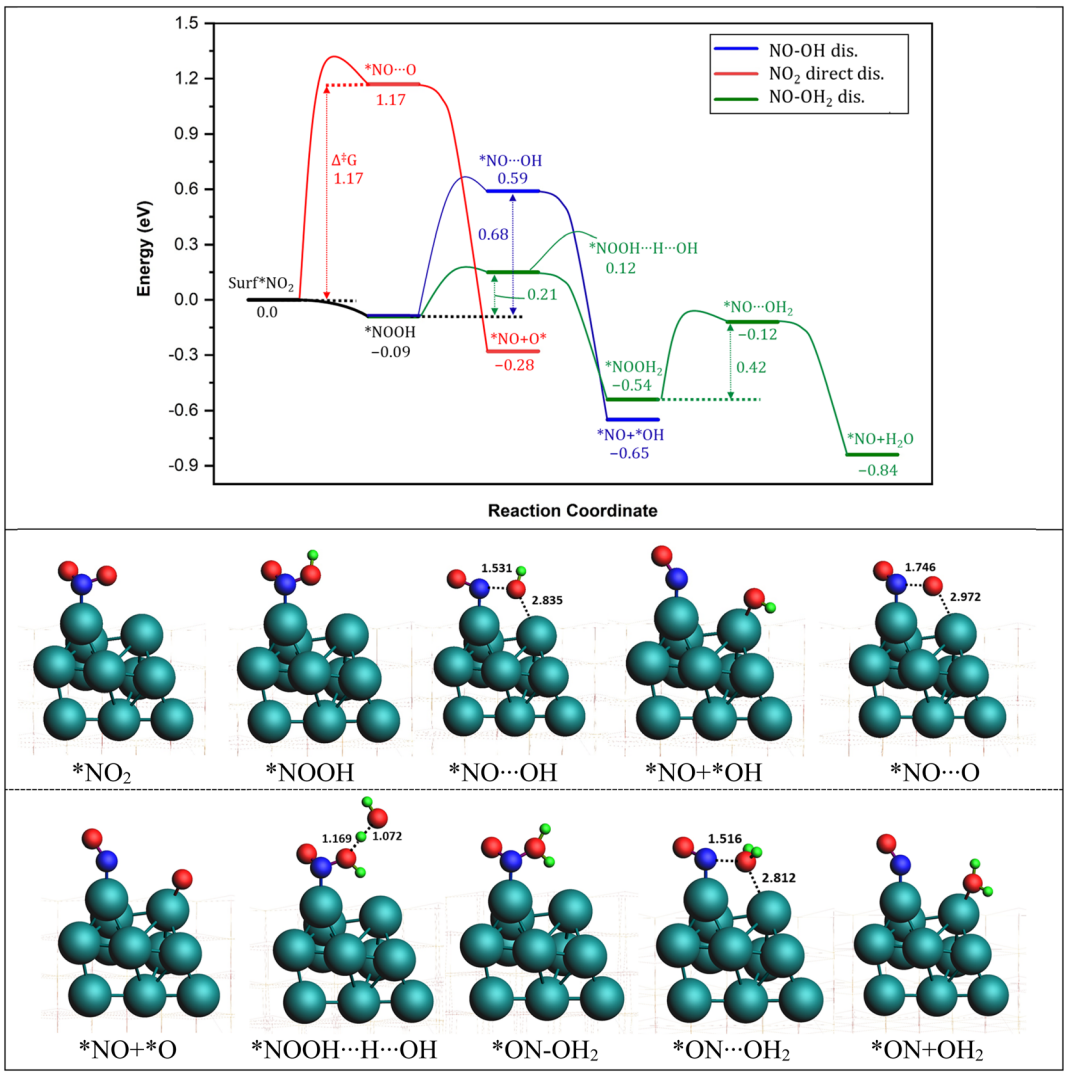

Fig. 3 (Top) reaction energy profile for the conversion pathway of NO_2 into NO. Green: NO–OH_2 dissociation, blue: NO–OH dissociation, red: NO_2 direct dissociation. The energy of the entering or leaving species was discounted from the total energy of the system to calculate the relative energy. The energy of the H was calculated as 1/2 of the energy of H_2. (Bottom) optimized structures of various intermediates and transition states involved in the reaction pathways. ZrO_2 layers are represented by wireframes for clarity. Energy values in eV. Bond distances in Å.

release of −0.84 eV, indicating that it is the most energetically favorable pathway for the conversion of $*NO_2$ into *NO. Based on the energy profiles in Fig. 3, it is evident that the most favorable pathway for the reduction of $*NO_2$ involves the sequential steps of $*NO_2 + *H_2 \rightarrow *ON{-}OH_2 + * \rightarrow *NO + *OH_2$. This pathway, which generates NO* as a key intermediate, is consistent with experimental findings reported by Chen *et al.*[76]

During the NO_3^- reduction process, the hydrogenation of $*NO_2$ plays a crucial role in the overall reaction. This hydrogenation occurs through an interesting mechanism known as the hydrogen shuttling model (HSM), wherein hydrogen is transferred *via* a nearby water molecule, acting as a bridge between $*NO_2$ and surface H*. This unique mechanism, allows for efficient hydrogenation reactions, however, in our case, the H is adsorbed on the surface quite strongly and hence can't be abstracted easily by the water molecule. Thus, the transition states could not be located for HSM mechanism. Therefore, we adopted the direct hydrogenation mechanism as the preferred approach for calculating the reaction energetics of hydrogenation steps in our work. This choice allows for a more accurate understanding of the hydrogenation reactions involved in the NO_3^- reduction on the ZrO_2 surface, enhancing our insights into the overall reaction mechanism and aiding in the development of efficient catalysts for nitrate reduction.

3.3. NO* reduction to $*NH_3$

In order to elucidate the mechanism and address the conflicting views regarding the conversion of NO* to NH_3 in experiments, we conducted comprehensive density functional theory (DFT) calculations to explore all possible pathways of NO* reduction to NH_3 with an aim to gain insights into the intricate pathways involved in this reduction process and determine the most favorable sequence of reactions. The reduction of NO* to NH_3 primarily entails two fundamental types of reactions: deoxygenation, involving the removal of oxygen, and nitrogen hydrogenation. The key challenge lies in determining the most favorable sequence of deoxygenation and hydrogenation steps. In Fig. 4, we present a summarized diagram illustrating the calculated energetics of the potential elementary steps, and the corresponding structures are presented in Fig. 5. Each of the four possible pathways is discussed below.

3.3.1 Direct NO* dissociation pathway. The direct dissociation of NO* into N* and O* exhibits a high energy barrier of 1.32 eV (Fig. 4). Subsequently, the N* species can be sequentially hydrogenated to NH_3*. Notably, the NH_x* species ($x = 1, 2$) preferentially captures a hydrogen atom directly to form NH_{x+1}* rather than *via* the hydrogen shuttling mechanism (HSM). The first hydrogenation of N* to *NH proceeds with a release of 0.14 eV of energy. Subsequent hydrogenation from *NH → $*NH_2$ → $*NH_3$ proceeds with activation energy barriers of 0.13 eV and 0.38 eV, respectively.

3.3.2 HN–O* dissociation pathway. The nitrogen end of NO* tends to undergo hydrogenation, forming HNO* *via* direct proton transfer with an exothermic reaction energy of −0.16 eV. However, the N–O bond in HNO* remains significantly strong, requiring a large dissociation reaction barrier of 0.91 eV to generate NH* and O*. Both of these product species remain attached to the Pt surface.

3.3.3 H_2N–O* dissociation pathway. In contrast, when the nitrogen end of NO* is doubly hydrogenated to form H_2N–O, the subsequent cleavage of N–O bond in H_2N–O becomes easier requiring a relatively smaller activation energy barrier of 0.48 eV comparing with larger $\Delta^{\ddagger}G$ of 0.91 and 1.32 eV in HN–O* dissociation and direct NO* dissociation pathways, respectively.

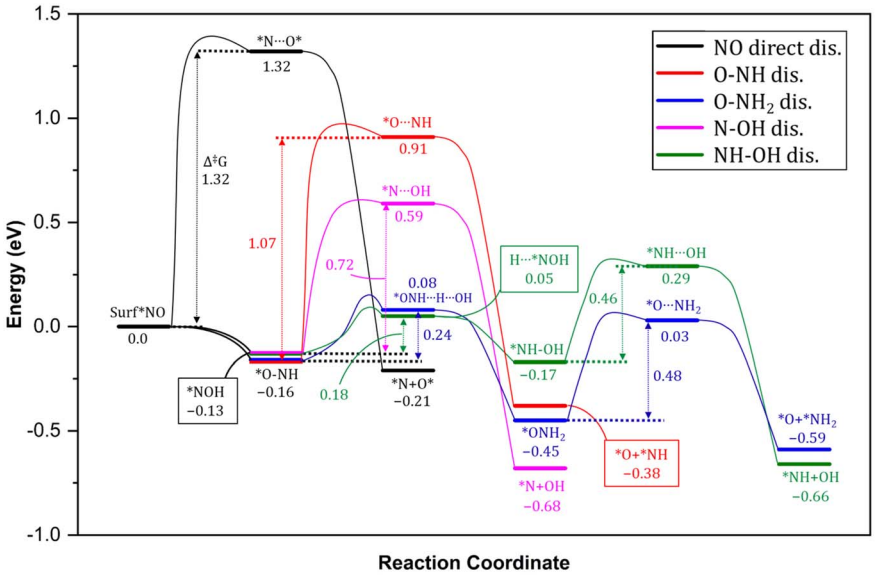

Fig. 4 Reaction energy profile for the conversion pathway of *NO into *N + O*. Green: NO–OH_2 dissociation, blue: NO–OH dissociation, red: NO_2 direct dissociation. The energy of the entering or leaving species were discounted from the total energy of the system to calculate the relative energy. The energy of the H was calculated as 1/2 of the energy of H_2. ZrO_2 layers are represented by wireframes for clarity. Energy values in eV. Bond distances in Å.

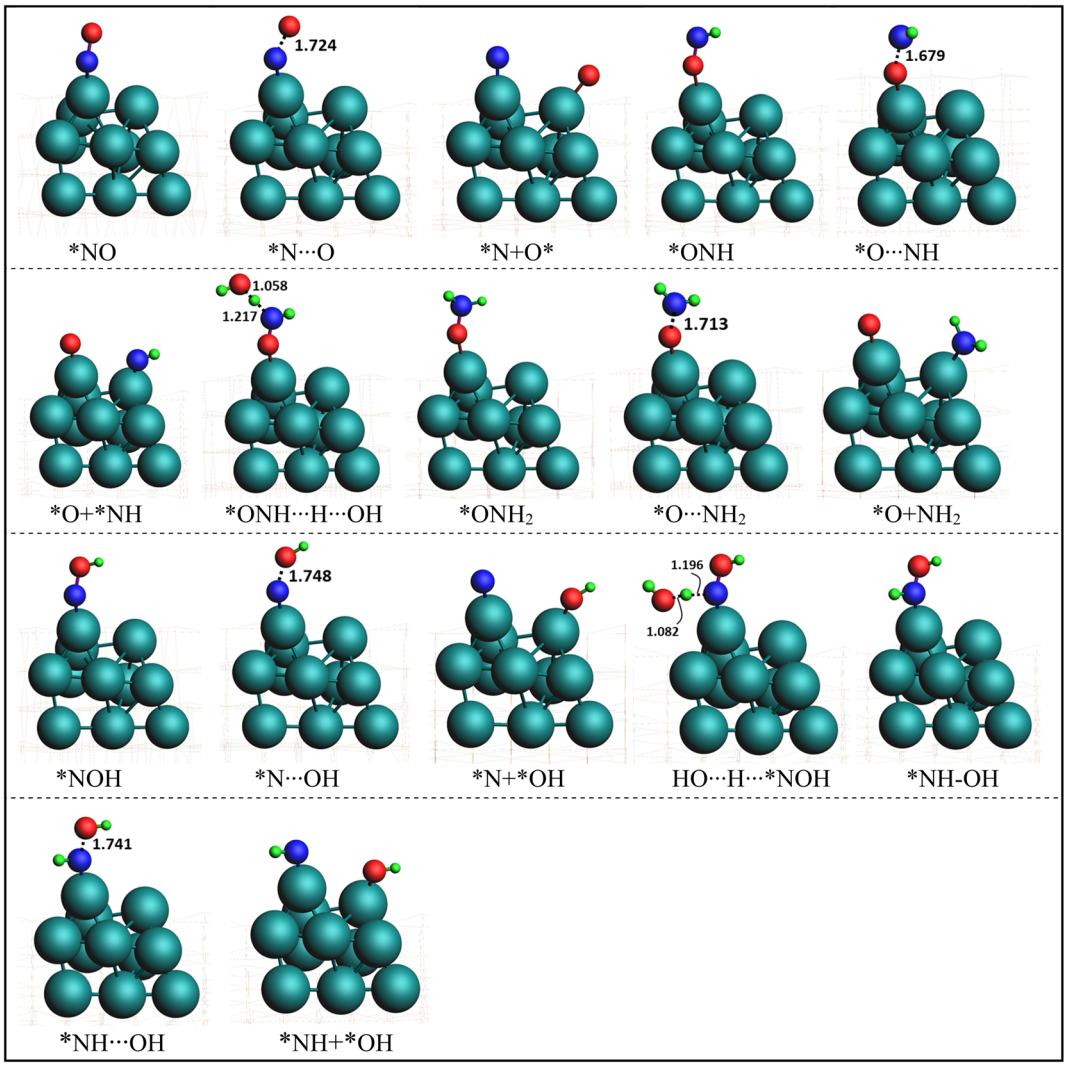

Fig. 5 Optimized geometries of various intermediate, transition states, and products involved in NO splitting into N and O. Geometries presented in the same order (with matching color names) as of reactions presentation in Fig. 4.

3.3.4 NH–OH* dissociation pathway. The hydrogenation of the oxygen end in HNO* proceeds with a minimal barrier of 0.13 eV, forming the HNOH* intermediate. Subsequently, the N–O bond in HN–OH* can be broken, leading to the formation of *NH and *OH species with a comparable (with H_2N–O* dissociation pathway requiring 0.48 eV) energy barrier of 0.46 eV and releasing a large energy of −0.81 eV. Although, this is apparently a more favourable pathway for the cleavage of N–O bond, however, the hydrogenation of O-end also requires a small barrier of 0.18 eV which is significantly lower in case of hydrogenation of N-end of NO. Finally, two successive hydrogenation steps can convert NH* into NH_3*.

3.3.5 N–OH* dissociation pathway. Alternatively, the hydrogenation of NO* can occur through the oxygen end. The resulting NOH* species can either break the N–OH bond to form N* and OH* with a large energy barrier of 0.72 eV and an energy release of −0.68 eV or the N-end of N–OH undergo hydrogenation and then follow the NH–OH* dissociation pathway which requires a smaller reaction barrier (0.46 *vs.* 0.72) to break the N–O bond compared to this pathway.

Thus, based on the above discussion and comparing the relative stability of intermediates, and products and the reaction energy barriers, the most favorable pathway for the cleavage of N–O bond and conversion on $PtNP/ZrO_2$ is either *NO → *NOH → HNOH* → HN + OH* or NO* → *ONH → H_2NO* → H_2N* + O*. The two calculated pathways compete with each requiring activation energy of 0.46 and 0.48 eV, respectively with comparable reaction exothermicity (0.66 *vs.* 0.59 eV). The calculated pathways are consistent with the nitrate reduction mechanism reported on the Pd surface by Shin *et al.*[77]

3.3.6 Overall picture. The most favorable overall pathway is presented in Fig. 6. The rate-determining step in this study is determined to be the cleavage of the N–O bond, which demands the highest activation energy. Among the potential pathways, direct NO dissociation stands as an unfavorable option due to its significantly elevated activation energy of 1.32 eV. In contrast, the more feasible route involves N–O bond cleavage

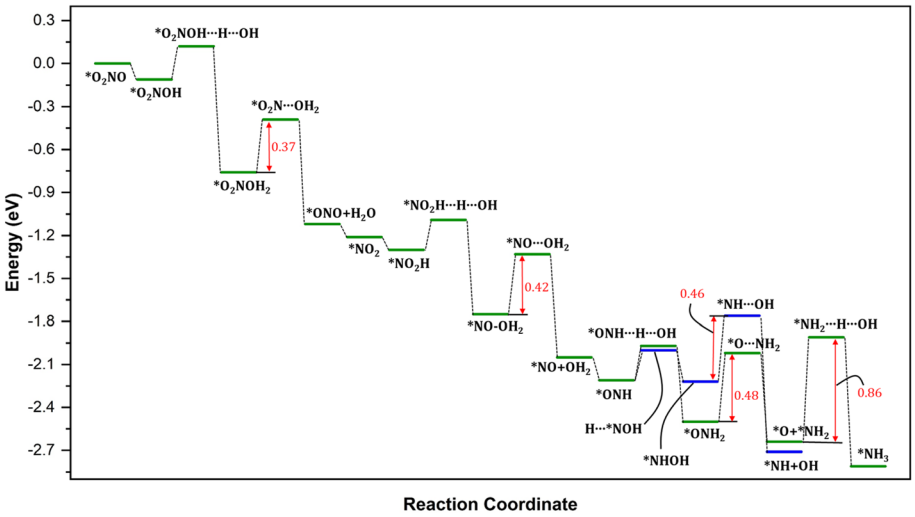

Fig. 6 Reaction energy profile for the overall pathway for the conversion of NO_3^- into NH_3 on the catalyst surface. Energy values in eV. The red vertical arrows represent the activation energy barriers for the rate-determining steps involved in the process. The energy of the entering or leaving species was discounted from the total energy of the system to calculate the relative energy. The energy of the H was calculated as 1/2 of the energy of H_2.

through hydrogenation at the oxygen end, necessitating an activation energy barrier ($\Delta^{\ddagger}G$) of 0.59 eV. Alternatively, when the nitrogen end of the NO group is initially hydrogenated, succeeded by N–O bond cleavage, NH_x ($x = 1, 2$) species emerge. The first hydrogenation step at the nitrogen end occurs spontaneously, devoid of a barrier, while the second hydrogenation step demands a modest energy input of 0.24 eV, resulting in the creation of *O–NH_x ($x = 1, 2$) intermediates. Subsequently, the rupture of the N–O bond in the formed *ONH_2 intermediate requires an activation energy of 0.48 eV. A third pathway, in which both the nitrogen and oxygen ends of NO are first hydrogenated, followed by N–O bond cleavage, presents an activation energy barrier of 0.46 eV. Consequently, the three pathways compete based on the activation energy barrier for the rate-determining step: N–O bond cleavage requiring 0.59, 0.48, and 0.46 eV for the first, second, and third pathways, respectively. The second and third pathways emerge as the most favorable options, with the third path exhibiting a slightly smaller activation energy barrier for N–O cleavage, thus holding particular promise.

To provide a comprehensive understanding of the NO_3^- reduction mechanism to NH_3 on the catalyst surface, we present the complete pathway in Fig. 6. It is evident that the overall process is highly exothermic, indicating that the reaction releases a significant amount of energy. Throughout the mechanism, we observe four notable energy barriers, as indicated by the red arrows.

The initial hydrogenation of N is energetically favorable without any barriers. The process of breaking the N–O in *N_x–OH_x ($x = 0, 1, 2$) intermediates leading to the formation of both *NH_x and *OH_x ($x = 0, 1, 2$) species requires significantly lower barriers. The resulting NH_x ($x = 0, 1, 2$) intermediate then undergoes hydrogenation to ultimately yield ammonia (*NH_3). Thus, considering the small reaction barriers and the large thermodynamic driving force, the production of *NH is expected to be a facile process. However, the subsequent hydrogenation step, *NH_2 + H → *NH_3, however, requires energy barriers of 0.86 eV. The large energy barrier for the hydrogenation leading to the formation of *NH_3 corresponds to the most energetically demanding steps in the entire mechanism and is, therefore, considered the rate-determining step (Fig. 6) in the formation of NH_3 after the cleavage of N–O bond. These findings suggest that the hydrogenation of NH_2* on the Pt surface is challenging, consistent with previous reports in the literature.[78,79] Breaking the N–O bond in NO on metal surfaces is known to have a notably high activation barrier, around 1.7 eV.[80–82] This means that under typical electro- and photochemical conditions, it is practically impossible to initiate this dissociation process. However, when NO is partially hydrogenated to form NOH*, the activation barrier to break the N–O bond is significantly lower, at approximately 0.9 eV. As further hydrogenation occurs, the activation barrier for dissociating HNOH* is even more reduced, reaching about 0.7 eV.[59,80–83] In simpler terms, the process becomes easier as you add hydrogen atoms. Notably, our calculated results demonstrate significantly lower activation energy barriers compared to those reported in the literature. Precisely, our calculations indicate that the direct N–O dissociation requires approximately 0.76–1.32 eV, and as the degree of hydrogenation increases, the activation energy barriers decrease further to approximately 0.62–0.98 eV for NH–OH intermediates and 0.37–0.42 eV for NO–OH_2 intermediates. These results are in line with those reported in literature, including the initial hydrogenation steps requiring very little energy.[59,80–84]

3.4. The rational design of the PtNP/ZrO_2 catalyst with metal doping

The design of highly efficient PtNP/ZrO_2 catalysts involves careful consideration of the metal-support interaction between the deposited Pt metal and the ZrO_2 support. This interaction

plays a critical role in determining the catalytic properties of the catalyst.[85–87] Metal/ZrO_2 systems are known for their strong metal-support interaction, resulting in charge redistribution at the metal-support interface. This charge redistribution significantly impacts the catalytic performance of the deposited Pt metal.[88,89] To modulate this metal-support interaction and alter the charge density of the Pt particles, we propose the promising approach of doping the ZrO_2 support with low-valence-state metals, that is, iron (Fe) and cobalt (Co).

By substituting Zr^{4+} cations with Fe^{2+} and Co^{2+} ions in the ZrO_2 lattice, we can effectively modify the charge distribution in the PtNP/ZrO_2 system. This strategic modification aims to induce electron density depletion in both the ZrO_2 support and the Pt cocatalyst, ultimately enhancing charge transfer and separation processes, which are crucial for improved catalytic activity. Experimental studies have demonstrated the feasibility and effectiveness of this doping approach in enhancing the catalytic performance of ZrO_2-based catalysts.[90–94] Introducing Fe or Co into the ZrO_2 lattice promotes electron density depletion in the Pt cocatalyst, leading to more efficient charge transfer and enhanced catalytic activity. Bader charge analyses indicate that the introduction of Fe^{2+} and Co^{2+} dopant ions cause the Pt_{11} cluster to gain a charge of +0.54 |e| and +0.46 |e|, respectively, compared to the undoped Pt_{11}/ZrO_2 (See Table 1 in SI).

To investigate the impact of Fe and Co doping on the PtNP/ZrO_2 catalyst, we constructed model catalysts, denoted as $Fe^{\#1}$–Pt/ZrO_2 and $Co^{\#1}$–Pt/ZrO_2, where Fe or Co was introduced as dopants, presented in Fig. 7. The dopants were placed away from the Pt cluster to focus solely on charge density regulation without introducing other effects. The dopants were placed at two other positions as well denoted as Fe/$Co^{\#2}$–Pt/ZrO_2 and Fe/$Co^{\#3}$–Pt/ZrO_2 and so on, as presented in Fig. S3,† however, this change of doping position has a negligible effect on the energetics.

To validate the feasibility of our approach, we conducted a thorough investigation of the energetics associated with key steps in the catalytic cycle, specifically focusing on the $*NO_3$ dissociation, and $*NH_2$ hydrogenation processes. We compared the results for the undoped Pt_{11} catalyst with those of the doped catalysts, $Fe^{\#1}$–Pt/ZrO_2 and $Co^{\#1}$–Pt/ZrO_2. Our analysis revealed that the $*NO_3$ dissociation over $Fe^{\#1}$–Pt/ZrO_2 and $Co^{\#1}$–Pt/ZrO_2 catalysts exhibited similar energetics to the undoped Pt_{11} catalyst. This implies that the introduction of Fe or Co dopants had minimal impact on the $*NO_3$ dissociation step. However, a significant improvement in the reaction barriers and energies was observed for the $*NH_2$ hydrogenation steps, which are the rate-determining steps in the catalytic cycle, upon Fe and Co doping. The incorporation of Fe or Co dopants led to a promotion of approximately 0.20 eV in the energetics of the $*NH_2$ hydrogenation steps, resulting in a more favorable and efficient catalytic process.

The observed improvements in the $*NH_2$ hydrogenation step upon Fe and Co doping provide strong evidence for the effectiveness of our rational design. The introduction of Fe or Co dopants into the ZrO_2 support induces electron density depletion in the Pt cocatalyst, facilitating the delivery of hydrogen to H-acceptor intermediates during the hydrogenation process, thereby promoting the overall catalytic activity. Importantly, similar reductions in hydrogen adsorption energy have been observed over other positively charged metals, such as Co, Ni, Cu, Pd, and Rh, corroborating the general principle for enhancing hydrogenation activity through charge density modulation.[95] It is crucial to note that due to the promotional effects of Fe and Co doping, the rate-determining $*NH_2$ hydrogenation step exhibits a relatively reduced energy barrier of 0.69 eV. This reduction underscores the effectiveness of doping in facilitating efficient hydrogenation during the nitrate-to-ammonia conversion over Pt-based catalysts. These findings emphasize the potential for enhanced catalytic performance and more sustainable ammonia production through the strategic use of doping techniques.

In the realm of catalysis, it is established that the coverage effect holds the potential to modify the bonding characteristics through interactions between adsorbed molecules. This phenomenon can notably influence the overall catalytic activity, particularly when dealing with materials that possess a substantial coverage of intermediate species.[96] In our study, we have also investigated the potential impact of the coverage effect on nitrate reduction, particularly focusing on the key rate-determining intermediate $*NH_2$. To assess the influence of adjacent $*NH_2$ on the surface, we calculated the reaction energetics of crucial processes involving dissociation and hydrogenation. By comparing the energetics obtained in the absence and presence of coadsorbed $*NH_2$, to explore the possible consequences of the coverage effect. The results, as shown in Table S2,† revealed several important findings. Firstly, for both $*NO_3$ and $*NO_2$ dissociation, the optimal pathway remains unchanged, occurring *via* the intermediates $*NO_2$–H_2O and *NO–OH rather than through direct dissociation. Secondly, although $*NH_2$ hydrogenation is mildly inhibited by the presence of neighboring $*NH_2$, the critical rate-determining $*NH_2$ hydrogenation step exhibits a notable effect, with a reduced barrier height of 0.11 eV and an increase in reaction energy by −0.13 eV (Table S2†). These findings suggest that the reaction mechanism may not be significantly altered when considering the coverage effect, and moreover, improved activity can be anticipated due to the enhanced energetics of the rate-determining step at high coverage. Regarding the formation of byproducts, our results indicate that the key intermediates

Table 1 Calculated activation energy barriers and reaction free energies for the five key rate-determining steps in nitrate reduction, for undoped neutral Pt_{11} and Fe- or Co-doped PtNP/ZrO_2, respectively. Energy values in eV

	Pt_{11} neutral		$Fe^{\#1}$–Pt/ZrO_2		$Co^{\#1}$–Pt/ZrO_2	
Major reactions	$\Delta^{\ddagger}G$	ΔG_r	$\Delta^{\ddagger}G$	ΔG_r	$\Delta^{\ddagger}G$	ΔG_r
O_2N–O diss.	0.37	−0.36	0.39	−0.37	0.36	−0.38
ON–O diss.	0.42	−0.30	0.41	−0.33	0.44	−0.31
N–O diss.	0.46	−0.14	0.45	−0.17	0.45	−0.15
HN–OH diss.	0.48	−0.49	0.49	−0.47	0.47	−0.51
$NH_2 \rightarrow NH_3$	0.87	−0.17	0.69	−0.24	0.71	−0.21

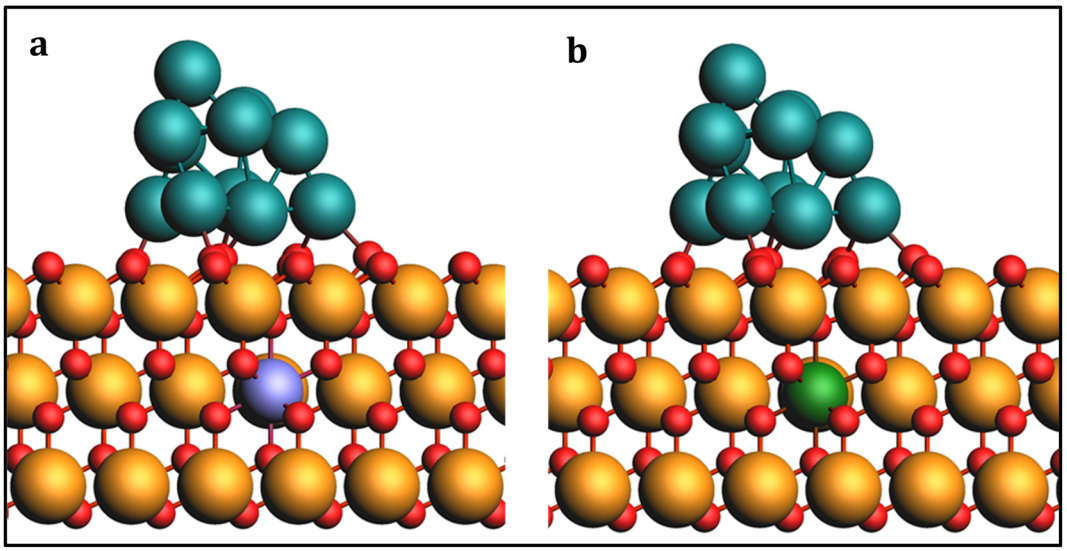

Fig. 7 Optimized geometries of (a) Fe and (b) Co-doped Pt_{11}/ZrO_2 structures. Light blue: Fe; green: Co.

*NO_2 and *NO are unlikely to be released due to their strong adsorption energies of −1.21 and −2.05 eV (Fig. 6), respectively, which is consistent with experimental observations.[19]

In summary, our study employed systematic density functional theory calculations to investigate the mechanism of nitrate reduction to ammonia over a $Pt_{11}/ZrO_2(111)$ catalyst. The following major conclusions were drawn:

(I) We identified the most favorable pathway for H*-assisted NO_3 reduction on $PtNP/ZrO_2$ as *NO_3 → *NO_2 → *NO → *ONH → *ONH_2/HNOH → *NH_2/NH → *NH_2 → *NH_3. Among the various reaction dissociation pathways, the cleavage of N–O bond and *NH_2 hydrogenation were found to have the highest barriers of 0.45 and 0.69 eV upon metal doping, respectively, indicating that N–O cleavage and *NH_2 hydrogenation are the rate-determining steps of the overall pathway.

(II) We observed distinct trends in the reaction energetics of dissociation and hydrogenation steps significantly influenced by metal-support interaction, driving charge redistribution at the interface. In light of this, we proposed a novel approach to modulate this metal-support interaction and to deplete the electron density of Pt by introducing low-valence-state metals, namely iron (Fe) and cobalt (Co), into the ZrO_2 support.

(III) We validated the effectiveness of the design strategy by demonstrating a significant promotion of approximately 0.20 eV in both the reaction barriers and energies of the rate-determining *NH_2 hydrogenation steps for $Fe–Pt/ZrO_2$ or $Co–Pt/ZrO_2$ compared to undoped $PtNP/ZrO_2$. This was attributed to the depletion of electron density within the Pt cocatalyst resulting in enhanced delivery of hydrogen to H-acceptor intermediates during the hydrogenation process, contributing to improved catalytic activity.

This study provides valuable insights into the catalytic activity of platinum-based ZrO_2 catalysts and their potential for reducing atmospheric pollutants, particularly NO_3, to valuable ammonia. The proposed doping approach holds the potential for the rational design of high-performance Pt-based catalysts for the reduction reactions on ZrO_2 support. While our study provides valuable insights into the catalytic mechanism of nitrate reduction over Pt nanoparticle-based ZrO_2, we acknowledge that the intricacies of charge density transfer to/from Na^+ ions and its nuanced effects on the interaction between Pt clusters and reaction intermediates represent aspects that may benefit from a more comprehensive investigation in future studies. These considerations are pivotal for refining our understanding of the complex interplay between catalyst composition, charge density variations, and catalytic activity. Nonetheless, our study not only contributes to the understanding of catalytic activity of platinum-based ZrO_2 catalysts but also offers a novel strategy for catalyst design to address atmospheric pollutant reduction. The presented results, insights, and proposed doping approach hold implications for advancing sustainable environmental protection and fostering cleaner and healthier environments.

Author contributions

Ayyaz Mahmood: conceptualization, writing – original draft, simulation, data collection, compilation, and discussion of results. Fouzia Perveen: manuscript revisions, funding acquisition. Tehmina Akram: writing and revising the manuscript. Shenggui Chen: formal analysis, project administration, funding acquisition. Ahmad Irfan: manuscript revisions, funding acquisition. Huafu Chen: formal analysis, project administration, funding acquisition.

Conflicts of interest

The authors declare that they have no known competing financial interests or personal relationships that could have appeared to influence the work reported in this paper.

Acknowledgements

This research is financially supported by the Key scientific research platforms and projects of Guangdong universities (2022ZDZX3064), the research project of Guangzhou Panyu Polytechnic (2023KJ04), the research platform of Guangzhou Panyu Polytechnic (2022KYPT03), the Guangzhou higher education teaching quality and teaching reform project (2022JSJXCXTD005 and 2022CXCYJH002). A. Irfan extends his appreciation to the Deanship of Scientific Research at King Khalid University for funding through large research groups program under grant number R.G.P.2/267/44.

References

1 J. Ângelo, L. Andrade, L. M. Madeira and A. Mendes, *J. Environ. Manage.*, 2013, **129**, 522–539.
2 R. Li, X. Mei, L. Chen, L. Wang, Z. Wang and Y. Jing, *Remote Sens.*, 2020, **12**, 1041.
3 S. Zhao, B. Hu, W. Gao, L. Li, W. Huang, L. Wang, Y. Yang, J. Liu, J. Li, D. Ji, R. Zhang, Y. Zhang and Y. Wang, *Atmos. Res.*, 2020, **241**, 104977.
4 N. Serpone, *Catalysts*, 2018, **8**, 553.
5 J. Lasek, Y.-H. Yu and J. C. S. Wu, *J. Photochem. Photobiol., C*, 2013, **14**, 29–52.
6 P. Warneck, *Chemistry of the Natural Atmosphere*, Academic Press, 1999, 2nd edn, vol. p. 71.
7 J. A. Last, W. M. Sun and H. Witschi, *Environ. Health Perspect.*, 1994, **102**, 179–184.
8 N. Gruber and J. N. Galloway, *Nature*, 2008, **451**, 293–296.
9 K. P. Cantor, *Cancer, Causes Control*, 1997, **8**, 292–308.
10 *Guidelines for Drinking-Water Quality, Third Edition, incorporating first and second addenda - World | ReliefWeb*, **https://reliefweb.int/report/world/guidelines-drinking-water-quality-third-edition-incorporating-first-and-second-addenda**, accessed July 8, 2023.
11 A. Menció, J. Mas-Pla, N. Otero, O. Regàs, M. Boy-Roura, R. Puig, J. Bach, C. Domènech, M. Zamorano, D. Brusi and A. Folch, *Sci. Total Environ.*, 2016, **539**, 241–251.
12 Y.-Y. Yang and G. S. Toor, *Water Res.*, 2017, **112**, 176–184.
13 R. Raja, G. Sankar and J. M. Thomas, *J. Am. Chem. Soc.*, 2001, **123**, 8153–8154.
14 H. Liu, X. Cao, L.-X. Ding and H. Wang, *Adv. Funct. Mater.*, 2022, **32**, 2111161.
15 V. Smil, *Nature*, 1999, **400**, 415.
16 J. M. McEnaney, A. R. Singh, J. A. Schwalbe, J. Kibsgaard, J. C. Lin, M. Cargnello, T. F. Jaramillo and J. K. Nørskov, *Energy Environ. Sci.*, 2017, **10**, 1621–1630.
17 G. Palmisano, V. Augugliaro, M. Pagliaro and L. Palmisano, *Chem. Commun.*, 2007, 3425–3437.
18 Y. Shiraishi and T. Hirai, *J. Photochem. Photobiol., C*, 2008, **9**, 157–170.
19 H. Hirakawa, M. Hashimoto, Y. Shiraishi and T. Hirai, *ACS Catal.*, 2017, **7**, 3713–3720.
20 H. Li, J. Shang, J. Shi, K. Zhao and L. Zhang, *Nanoscale*, 2016, **8**, 1986–1993.
21 T. Oshikiri, K. Ueno and H. Misawa, *Angew. Chem., Int. Ed.*, 2014, **53**, 9802–9805.
22 A. Takai and P. V. Kamat, *ACS Nano*, 2011, **5**, 7369–7376.
23 N. Chandrasekharan and P. V. Kamat, *J. Phys. Chem. B*, 2000, **104**, 10851–10857.
24 R. Kato, M. Furukawa, I. Tateishi, H. Katsumata and S. Kaneco, *ChemEngineering*, 2019, **3**, 49.
25 M. Yamauchi, R. Abe, T. Tsukuda, K. Kato and M. Takata, *J. Am. Chem. Soc.*, 2011, **133**, 1150–1152.
26 G. Prieto, J. Zečević, H. Friedrich, K. P. de Jong and P. E. de Jongh, *Nat. Mater.*, 2013, **12**, 34–39.
27 S. Kattel, W. Yu, X. Yang, B. Yan, Y. Huang, W. Wan, P. Liu and J. G. Chen, *Angew. Chem., Int. Ed.*, 2016, **55**, 7968–7973.
28 K. Larmier, W.-C. Liao, S. Tada, E. Lam, R. Verel, A. Bansode, A. Urakawa, A. Comas-Vives and C. Copéret, *Angew. Chem., Int. Ed.*, 2017, **56**, 2318–2323.
29 K. W. Ting, T. Toyao, S. M. A. H. Siddiki and K. Shimizu, *ACS Catal.*, 2019, **9**, 3685–3693.
30 B. C. Sempuga and Y. Yao, *J. CO2 Util.*, 2017, **20**, 34–42.
31 J. Wambach, A. Baiker and A. Wokaun, *Phys. Chem. Chem. Phys.*, 1999, **1**, 5071–5080.
32 M. M.-J. Li and S. C. E. Tsang, *Catal. Sci. Technol.*, 2018, **8**, 3450–3464.
33 K. Jalama, *Catal. Rev.*, 2017, **59**, 95–164.
34 M. D'Arino, F. Pinna and G. Strukul, *Appl. Catal., B*, 2004, **53**, 161–168.
35 Y. Zhang, J. Fei, Y. Yu and X. Zheng, *Energy Convers. Manage.*, 2006, **47**, 3360–3367.
36 V. I. Bogdan, A. E. Koklin, S. A. Nikolaev and L. M. Kustov, *Top. Catal.*, 2016, **59**, 1104–1109.
37 T. Phongamwong, U. Chantaprasertporn, T. Witoon, T. Numpilai, Y. Poo-arporn, W. Limphirat, W. Donphai, P. Dittanet, M. Chareonpanich and J. Limtrakul, *Chem. Eng. J.*, 2017, **316**, 692–703.
38 J. Lin, C. Ma, Q. Wang, Y. Xu, G. Ma, J. Wang, H. Wang, C. Dong, C. Zhang and M. Ding, *Appl. Catal., B*, 2019, **243**, 262–272.
39 M. Romero-Sáez, A. B. Dongil, N. Benito, R. Espinoza-González, N. Escalona and F. Gracia, *Appl. Catal., B*, 2018, **237**, 817–825.
40 C. Chen, C. Ruan, Y. Zhan, X. Lin, Q. Zheng and K. Wei, *Int. J. Hydrogen Energy*, 2014, **39**, 317–324.
41 M. M. Kauppinen, M. M. Melander, A. S. Bazhenov and K. Honkala, *ACS Catal.*, 2018, **8**, 11633–11647.
42 X. Yao, L. Chen, J. Cao, Y. Chen, M. Tian, F. Yang, J. Sun, C. Tang and L. Dong, *Chem. Eng. J.*, 2019, **369**, 46–56.
43 S. Liu, H. Wang, Y. Wei, R. Zhang and S. Royer, *ACS Appl. Mater. Interfaces*, 2019, **11**, 22240–22254.
44 Y. Okamoto and H. Gotoh, *Catal. Today*, 1997, **36**, 71–79.
45 H. Koga, A. Hayashi, Y. Ato, K. Tada, S. Hosokawa, T. Tanaka and M. Okumura, *Catal. Today*, 2019, **332**, 236–244.
46 M.-fei Luo, Yi-jun Zhong, Bo Zhu, X.-xin Yuan and X.-ming Zheng, *Appl. Surf. Sci.*, 1997, **115**, 185–189.
47 C. Sun, J. Zhu, Y. Lv, L. Qi, B. Liu, F. Gao, K. Sun, L. Dong and Y. Chen, *Appl. Catal., B*, 2011, **103**, 206–220.
48 H. Koga, K. Tada, A. Hayashi, Y. Ato and M. Okumura, *Catal. Lett.*, 2017, **147**, 1827–1833.

49 J. Xing, Y. H. Li, H. B. Jiang, Y. Wang and H. G. Yang, *Int. J. Hydrogen Energy*, 2014, **39**, 1237–1242.
50 D. Wang, Z.-P. Liu and W.-M. Yang, *ACS Catal.*, 2018, **8**, 7270–7278.
51 J. K. Nørskov, T. Bligaard, A. Logadottir, J. R. Kitchin, J. G. Chen, S. Pandelov and U. Stimming, *J. Electrochem. Soc.*, 2005, **152**, J23.
52 J. Greeley, T. F. Jaramillo, J. Bonde, I. Chorkendorff and J. K. Nørskov, *Nat. Mater.*, 2006, **5**, 909–913.
53 Q.-H. Zhang, W.-D. Han, Y.-J. Hong and J.-G. Yu, *Catal. Today*, 2009, **148**, 335–340.
54 C. Dong, C. Lian, S. Hu, Z. Deng, J. Gong, M. Li, H. Liu, M. Xing and J. Zhang, *Nat. Commun.*, 2018, **9**, 1252.
55 Y. Ji and Y. Luo, *ACS Catal.*, 2016, **6**, 2018–2025.
56 G. A. Cerrón-Calle, A. S. Fajardo, C. M. Sánchez-Sánchez and S. Garcia-Segura, *Appl. Catal., B*, 2022, **302**, 120844.
57 G. E. Dima, A. C. A. de Vooys and M. T. M. Koper, *J. Electroanal. Chem.*, 2003, **554–555**, 15–23.
58 M. C. Figueiredo, J. Souza-Garcia, V. Climent and J. M. Feliu, *Electrochem. Commun.*, 2009, **11**, 1760–1763.
59 A. Clayborne, H.-J. Chun, R. B. Rankin and J. Greeley, *Angew. Chem.*, 2015, **127**, 8373–8376.
60 V. Rosca, G. L. Beltramo and M. T. M. Koper, *Langmuir*, 2005, **21**, 1448–1456.
61 A. Cuesta and M. Escudero, *Phys. Chem. Chem. Phys.*, 2008, **10**, 3628–3634.
62 A. Mahmood, T. Akram, C. Shenggui and C. Huafu, *Int. J. Hydrogen Energy*, 2023, under review.
63 M. Franchini, P. H. T. Philipsen, E. van Lenthe and L. Visscher, *J. Chem. Theory Comput.*, 2014, **10**, 1994–2004.
64 P. H. T. Philipsen, G. te Velde, E. J. Baerends, J. A. Berger, P. L. de Boeij, M. Franchini, J. A. Groeneveld, E. S. Kadantsev, R. Klooster, F. Kootstra, P. Romaniello, M. Raupach, D. G. Skachkov, J. G. Snijders, C. J. O. Verzijl, J. A. Celis Gil, J. M. Thijssen, G. Wiesenekker and T. Ziegler, *BAND202 SCM*, Theoretical Chemistry, Vrije Universiteit, Amsterdam, The Netherlands, 2023.
65 G. te Velde, F. M. Bickelhaupt, E. J. Baerends, C. Fonseca Guerra, S. J. A. van Gisbergen, J. G. Snijders and T. Ziegler, *J. Comput. Chem.*, 2001, **22**, 931–967.
66 J. P. Perdew, K. Burke and M. Ernzerhof, *Phys. Rev. Lett.*, 1996, **77**, 3865–3868.
67 Y. Zhang and W. Yang, *Phys. Rev. Lett.*, 1998, **80**, 890.
68 S. Grimme, J. Antony, S. Ehrlich and H. Krieg, *J. Chem. Phys.*, 2010, **132**, 154104.
69 H. J. Monkhorst and J. D. Pack, *Phys. Rev. B*, 1976, **13**, 5188–5192.
70 A. Mahmood, T. Akram, M. Kiani, X. Tian and Y. Sun, *New J. Chem.*, 2023, **46**, 16593–16602.
71 A Mahmood, E. S. Teixeira and R. L. Longo, *J. Org. Chem.*, 2015, **80**(16), 8198–8205.
72 A. Mahmood and R. L. Longo, *Phys Chem Chem Phys*, 2016, **18**(25), 17062–17070.
73 S. Hammond, *J. Am. Chem. Soc.*, 1955, **77**, 334.
74 R. Jia, Y. Wang, C. Wang, Y. Ling, Y. Yu and B. Zhang, *ACS Catal.*, 2020, **10**, 3533–3540.
75 Z.-Y. Wu, M. Karamad, X. Yong, Q. Huang, D. A. Cullen, P. Zhu, C. Xia, Q. Xiao, M. Shakouri, F.-Y. Chen, J. Y. (Timothy) Kim, Y. Xia, K. Heck, Y. Hu, M. S. Wong, Q. Li, I. Gates, S. Siahrostami and H. Wang, *Nat. Commun.*, 2021, **12**, 2870.
76 G.-F. Chen, Y. Yuan, H. Jiang, S.-Y. Ren, L.-X. Ding, L. Ma, T. Wu, J. Lu and H. Wang, *Nat. Energy*, 2020, **5**, 605–613.
77 H. Shin, S. Jung, S. Bae, W. Lee and H. Kim, *Environ. Sci. Technol.*, 2014, **48**, 12768–12774.
78 Y. Wang, H. Li, W. Zhou, X. Zhang, B. Zhang and Y. Yu, *Angew. Chem., Int. Ed.*, 2022, **61**, e202202604.
79 Y. Wang, A. Xu, Z. Wang, L. Huang, J. Li, F. Li, J. Wicks, M. Luo, D.-H. Nam, C.-S. Tan, Y. Ding, J. Wu, Y. Lum, C.-T. Dinh, D. Sinton, G. Zheng and E. H. Sargent, *J. Am. Chem. Soc.*, 2020, **142**, 5702–5708.
80 Z.-H. Zeng, J. L. F. Da Silva, H.-Q. Deng and W.-X. Li, *Phys. Rev. B*, 2009, **79**, 205413.
81 M. Gajdoš, J. Hafner and A. Eichler, *J. Phys.: Condens. Matter*, 2005, **18**, 41.
82 C. A. Farberow, J. A. Dumesic and M. Mavrikakis, *ACS Catal.*, 2014, **4**, 3307–3319.
83 C. A. Casey-Stevens, H. Ásmundsson, E. Skúlason and A. L. Garden, *Appl. Surf. Sci.*, 2021, **552**, 149063.
84 T. Hu, C. Wang, M. Wang, C. M. Li and C. Guo, *ACS Catal.*, 2021, **11**, 14417–14427.
85 M. Ali, E. Pervaiz, U. Sikandar and Y. Khan, *Int. J. Hydrogen Energy*, 2021, **46**, 18257–18283.
86 Z. Li, L. Zhai, T. Ma, J. Zhang and Z. Wang, *Catalysts*, 2022, **12**, 1385.
87 A. M. Ruppert, M. Niewiadomski, J. Grams and W. Kwapiński, *Appl. Catal., B*, 2014, **145**, 85–90.
88 R. Wang, K. Wang, H. Wang, Q. Wang, J. Key, V. Linkov and S. Ji, *Int. J. Hydrogen Energy*, 2013, **38**, 5783–5788.
89 A. Perechodjuk, Y. Zhang, V. A. Kondratenko, U. Rodemerck, D. Linke, S. Bartling, C. R. Kreyenschulte, G. Jiang and E. V. Kondratenko, *Appl. Catal., A*, 2020, **602**, 117731.
90 Q. Cheng, W. Yang, Q. Chen, J. Zhu, D. Li, L. Fu and L. Zhou, *Appl. Surf. Sci.*, 2020, **530**, 147291.
91 P. Ghigna, G. Spinolo, U. Anselmi-Tamburini, F. Maglia, M. Dapiaggi, G. Spina and L. Cianchi, *J. Am. Chem. Soc.*, 1999, **121**, 301–307.
92 H. Song, J. A. Hong, H. Lee and K. Lim, *Sci. Rep.*, 2019, **9**, 10965.
93 W. Ahmed and J. Iqbal, *Ceram. Int.*, 2020, **46**, 25833–25844.
94 F. G. Pinto, M. A. Paulin, A. G. Leyva and J. Sacanell, *Mater. Res. Express*, 2018, **5**, 066103.
95 D. Wang, Z.-P. Liu and W.-M. Yang, *ACS Catal.*, 2017, **7**, 2744–2752.
96 A. C. Lausche, A. J. Medford, T. S. Khan, Y. Xu, T. Bligaard, F. Abild-Pedersen, J. K. Nørskov and F. Studt, *J. Catal.*, 2013, **307**, 275–282.